High-throughput flow alignment of barcoded hydrogel microparticles†

Stephen C. Chapin, Daniel C. Pregibon and Patrick S. Doyle*

Received 20th May 2009, Accepted 24th July 2009
First published as an Advance Article on the web 11th August 2009
DOI: 10.1039/b909959j

Suspension (particle-based) arrays offer several advantages over conventional planar arrays in the detection and quantification of biomolecules, including the use of smaller sample volumes, more favorable probe-target binding kinetics, and rapid probe-set modification. We present a microfluidic system for the rapid alignment of multifunctional hydrogel microparticles designed to bear one or several biomolecule probe regions, as well as a graphical code to identify the embedded probes. Using high-speed imaging, we have developed and optimized a flow-through system that (1) allows for a high particle throughput, (2) ensures proper particle alignment for decoding and target quantification, and (3) can be reliably operated continuously without clogging. A tapered channel flanked by side focusing streams is used to orient the flexible, tablet-shaped particles into a well-ordered flow in the center of the channel. The effects of channel geometry, particle geometry, particle composition, particle loading density, and barcode design are explored to determine the best combination for eventual use in biological assays. Particles in the optimized system move at velocities of ~50 cm s^{-1} and with throughputs of ~40 particles s^{-1}. Simple physical models and CFD simulations have been used to investigate flow behavior in the device.

Introduction

The ability to accurately detect and quantify biological molecules in a complex mixture is crucial in both basic research and clinical settings. Advancements in the fields of genomics and proteomics require robust technologies that can obtain high-density information from biological samples in a rapid and cost-effective manner.[1–4] High-throughput screening for genetic analysis, combinatorial chemistry, and clinical diagnostics benefits greatly from multiplexed analysis,[5,6] which is the simultaneous detection of several target molecules. This approach significantly reduces the required assay time, sample volume, and cost. However, it requires an encoding scheme that can be used during analysis to identify immobilized probe species.

Particle-based assay platforms exhibit several advantages over planar arrays in applications that involve the detection of low to medium target densities (1–1000), demand rapid probe-set modification, or necessitate high-throughput processing of samples.[7] Compared to planar arrays, the use of micrometer-sized particles leads to faster probe-target binding kinetics due to mixing during incubation, more efficient separation and washing steps, and higher degrees of reproducibility.[8,9] The vast majority of particles used in suspension arrays are optically encoded latex microspheres with diameters between 0.3 and 10 μm that can be interrogated and decoded with laser-based flow cytometry. Optical encoding is accomplished by swelling the spheres with fluorescent organic dyes with different emission spectra. Although used extensively, this scheme requires multiple excitations and is limited to the multiplexed sensing of only ~100 analytes due to spectral overlap of encoding and analyte-detection fluorescence.[10,11] Submicrometer rods with multiple metal stripes that serve as a graphical code for multiplexing have also been developed,[12,13] but the high density of such rods leads to rapid settling in solution and thus requires the rods to be vigorously mixed during assays, a procedure which can damage fragile biological molecules like antibodies. Moreover, a feasible high-throughput quantification and decoding strategy for the rods has never been introduced, thereby significantly limiting their applicability in clinical or research settings.

Recently, innovations in gel-based microchips[14] were combined with suspension array technology to create multifunctional, graphically-encoded hydrogel microparticles for biomolecule analysis.[15] Implementing photolithography and microfluidic-based techniques,[16] geometrically and chemically complex microparticles were rapidly synthesized (10^4 h^{-1}) with high reproducibility from co-flowing streams of UV-curable monomers. Synthesis, encoding, and functionalization of the particles occurred in a single step, with unpolymerized holes in the wafer structure used to construct a 20-bit fluorescent "barcode" region. Multiplexed detection of fluorescently labeled DNA oligomers was demonstrated with high specificity, high sensitivity, and short hybridization times. Nonspecific binding in multiplexed assays was minimized through the use of a biocompatible and non-fouling poly(ethylene glycol) (PEG) polymer scaffold. Compared to the surface immobilization strategies employed with planar arrays and latex microspheres, the immobilization of probe molecules in a three-dimensional gel structure leads to more favorable hybridization kinetics due to the hydrated environment, high probe-loading densities, and decreased steric hindrance.[17] Furthermore, the physical separation of code and probe regions on each particle enables the use of

---

Department of Chemical Engineering, MIT 66-053, 77 Massachusetts Ave., Cambridge, MA, 02139, USA. E-mail: pdoyle@mit.edu

† Electronic supplementary information (ESI) available: High-speed movies showing particles moving through detection zone and focusing stages. Details of modeling and lubrication approximation. See DOI: 10.1039/b909959j

a common fluorophore for all signaling purposes, thus avoiding the spectral issues that limit the multiplexing capacity of the optical encoding schemes discussed earlier and also reducing the costs associated with detection equipment. Although flow-through scanning was demonstrated for a limited number of encoded hydrogel particles,[15] the processing rate was low (<1 particle s^{-1}) and therefore not suitable for high-throughput applications. Robustness of the device was also not explored.

Originally developed in the 1950s to count cells,[18] flow cytometry has become a versatile tool for the rapid interrogation of the synthetic microparticles used in suspension arrays.[19,20] Compact and inexpensive molded microfluidic cytometers made of the silicone elastomer poly(dimethylsiloxane) (PDMS) have been developed for particle sizing, as well as single-line fluorescence detection.[21,22] The ability to achieve well-ordered flows with uniform particle velocity and passage time is essential for accurate detection and characterization in such devices. The most common method of directing the particles through the channel involves the hydrodynamic focusing of the particle-bearing stream with secondary sheath flows.[23,24] Recent advances have led to high-throughput and high-resolution cytometers capable of three-dimensional hydrodynamic focusing.[25,26]

In order to extend the barcoded hydrogel platform to real-world applications in high-throughput screening, we seek to develop a robust microfluidic approach to the rapid interrogation of each particle. We present a parametric study to understand the various geometric, mechanical, and operating factors that govern the system's performance. The inclusion of properly-spaced side-focusing streams, the use of a sufficiently wide detection zone, the modulation of particle cross-link density and morphology, and the choice of particle loading concentration were identified as the most crucial elements. We demonstrate here a new system that implements the design principles distilled from this study and thereby is capable of reliably manipulating the relatively large and flexible hydrogel particles into a single-file, high-velocity procession without clogging or deformation. The ability to align particles in the channel with high precision will enable future photomultiplier tube (PMT)-based detection with a simple one-dimensional line scan that integrates fluorescence intensity along a thin excitation beam established perpendicular to the flow direction of the particle. The resulting profile could then be used to reconstruct the identity of the particle as well as the extent of the binding events on the various probe and control regions.

Theory

The tablet-shaped hydrogel particles investigated here are substantially larger (~250 × ~80 × ~35 μm, Fig. 1a) and more flexible than the latex microspheres commonly used in other suspension arrays. This introduces additional design considerations regarding flow velocity and mechanical stress. Pressure-driven flow is used to carry the particles through rectangular PDMS channels, while sets of side streams and abrupt contractions in width serve to orient the particles prior to their entrance into a narrow "detection zone." In a rectangular channel with a high cross-sectional aspect ratio, it is expected that a parabolic velocity distribution will develop along the small dimension. This flow profile can inhibit the performance of cytometers by generating nonuniform particle velocities. Although the short dimension can be further reduced to physically confine the particles, this lowers flow velocity and throughput. Higher driving pressures could be used to counteract these decreases, but such an approach may lead to deformation of the channel and/or the particles. While the velocity distribution in the long cross-sectional dimension will be nearly uniform in the center of the channel, large gradients will develop in a layer near the wall. Particles passing through this layer will be slowed significantly. Focusing streams and periodic contractions in channel width could be used to disturb the developed flow along the walls and eject particles into the central flow region for better cytometric performance. It has previously been shown that rapid decreases of channel cross-section can enhance the focusing of deformable blood cells by introducing regions of high shear rate adjacent to the walls that produce strong hydrodynamic lift forces.[27]

The pressure-driven flow of both rigid and flexible disk-shaped bodies in parallel plate channels has been used to model the behavior of red blood cells in certain microvessels in which cell and passage heights are nearly equal.[28,29] Although the mechanical properties of cells and hydrogels differ in some aspects, many of the effects observed in these studies are relevant to the current investigation. For flexible bodies that deform at constant volume and surface area, it was found that the pressure in the thin "height gaps" above and below the body (Fig. 1b) will be uniform. Small deformations in the body height were shown to produce a gap distance that varied with spanwise (y) position only; the gap distance was constant along lines parallel to the flow. Cell velocity was predicted to be much less than that of the bulk fluid for channels with small height gaps and with spans

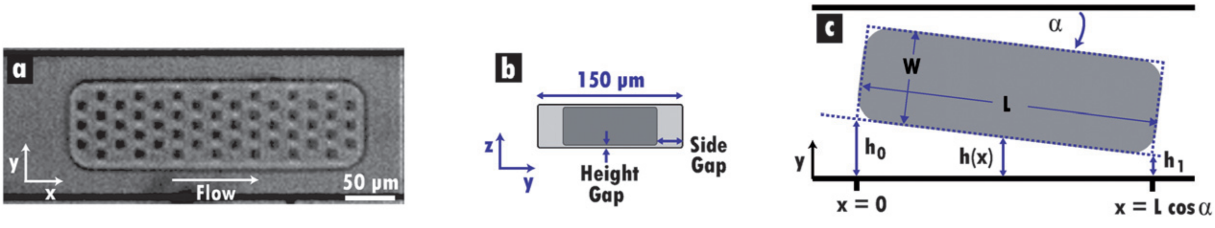

Fig. 1 Particle flow in rectangular channels. (a) Image from high-speed movie of model particle flowing "lengthwise" at 30 cm s^{-1} from left to right in 150 μm wide channel. Columns of coding holes run in the y-direction, while rows run in the x-direction. (b) Cross-sectional schematic of the particle in (a). The height gap is ~1–2 μm in the studies presented. The larger side gap permits significant bypass flow, thus leading to bulk fluid velocities that are higher than particle velocities. (c) Schematic of pertinent variables for application of the lubrication approximation to analyze lift forces and torques on misaligned particles in channel regions where side-gap flow is nearly unidirectional.

much larger than cell width. This effect can be attributed to the ability of the fluid to easily bypass the cell by moving through the relatively large "side gaps." In contrast, for tightly fitting bodies in cylindrical tubes, the driving pressure is concentrated across the particle, leading to bulk fluid velocities that are lower than body velocities and even "leakback" of fluid.[30]

A thorough understanding of the hydrodynamic forces that act on the particles in the channel is crucial for the development of an effective cytometry system. For the narrow detection portions of the channel a lubrication approximation can be utilized to determine the lift forces on a particle that arise from the bypass flow in the side gaps just described (see ESI†). This analysis can be used to rationally design a particle and a channel that will give rise to forces and torques that most effectively position and align the particle for proper scanning. In a reference frame moving with the particle, the fluid velocity and pressure drop in the side gap are given by:

$$v_x(x,y) = \frac{y}{2\mu}\frac{dP}{dx}\big(y-h(x)\big) + U_w\left(\frac{y}{h(x)}-1\right) \tag{1}$$

$$\frac{dP}{dx} = -\frac{12\mu q}{h(x)^3} - \frac{6\mu U_w}{h(x)^2} \tag{2}$$

where μ is the dynamic viscosity, P is the dynamic pressure, U_w is the wall velocity, and q is the volumetric flow rate per unit width (see Fig. 1c for other definitions). The geometric and dynamic criteria required for application of the lubrication analysis become $tan\ \alpha \ll 1$ and $(q/v)\ tan\ \alpha \ll 1$.[31] Neglecting deformation and any three-dimensional effects from flow in the height gap, these conditions are met by the nearly unidirectional bypass flow established in the side gaps when an oblong particle is passing through the relatively narrow regions of the channel at small α. In analyzing the stress exerted by the fluid on a rigid particle surface, the normal viscous stresses are zero, and the components of the stress vector are thus given by:

$$s_x = -\frac{dh}{dx}P - \mu\frac{\partial v_x}{\partial y} \tag{3}$$

$$s_y = P \tag{4}$$

The torque (per unit width) about $\mathbf{r_0}$ can be calculated as

$$\mathbf{G} = \int_{x_1}^{x_2} (\mathbf{r}\text{-}\mathbf{r}_0) \times \mathbf{s}(\mathbf{n})\mathrm{d}x \tag{5}$$

Meanwhile, the rotational and translational tendencies of particles in the wider regions of the channel (*i.e.*, upstream) are best understood by the principle of gradient minimization, which dictates that the oblong particles will tend to rotate until the velocity gradient across their rear surface can no longer be reduced. For rectangular particles with high aspect ratios, this condition will be met once the short and long dimensions have been oriented perpendicular and parallel, respectively, to the flow direction. The large particles used in the study are expected to impact the time scale of this orientation process by altering local velocity profiles and generating significant wake flows in areas of high particle concentration.

Materials and methods

Soft lithography and device fabrication

The microfluidic devices used to synthesize particles and to generate ordered particle flows were fabricated in PDMS (Sylgard 184, Dow Corning) using soft lithography methods (ESI†). Channels used for particle synthesis had heights between 37.4 and 39.9 μm, while those used for particle flowing were between 38.2 and 38.6 μm in height.

Particle synthesis

Hydrogel microparticles were photopolymerized at rates up to 18 000 h^{-1} with 75 ms UV exposures using the stop-flow lithography (SFL) method.[16] A power meter (Newport, Model 1815-C) and appropriate adjustment of the lamp strength were used to ensure a consistent UV intensity (0.8 μW mm^{-2}) during the course of the experiments. This step was taken to avoid unexpected variations in polymerization extent due to the intensity changes over the lifetime of the mercury bulb. Microfluidic devices with 1–4 inlets were connected to a compressed air source by Tygon tubing with modified 10 and 200 μl pipette tips (Biosciences) attached to one end.

Two different prepolymer solutions, "DA20" and "DA30," were used in the course of the experiments; the composition of each is given in Table 1. Prepolymer solutions were mixed 9 : 1 with 1× TE to mimic the monomer formulation used in previous nucleic acid detection experiments. When synthesizing particles with multiple chemistries, food coloring was added to the DA30 at 2% of the final monomer solution volume to create a contrast difference that could be exploited for stream visualization in the synthesis process using a CCD camera (KP-M1A, Hitachi). Atomic force microscopy (AFM) was used to determine the elastic moduli of particles synthesized with DA20 and DA30 (ESI†).

Particles were flushed down the synthesis channel and collected in a 0.6 μl Eppendorf tube filled with 300 μl of TET (1× TE with 0.05% (v/v) Tween-20 surfactant (Sigma Aldrich)). TET was then used to rinse the particles of unreacted monomer as well as PEG and food coloring in a series of five washing steps that involved manual aspiration facilitated by centrifugal separation of the dense particles. Particles were stored in TET at final concentrations of ~10 particles μl^{-1} in a refrigerator (4 °C). Unless otherwise noted, particle dimensions cited in the paper refer to the size expected from the transparency mask used. The length of each dimension could be up to 4% greater for particles made from DA20 due to swelling.

Flow device operation

Flow devices with two inlets and one outlet were used for all experiments (Fig. 2). Prior to being loaded into the flow device,

Table 1 Composition (v/v) of prepolymers used in particle synthesis

	DA20	DA30
Poly(ethylene glycol) (MW = 700) diacrylate (PEG-DA)	20%	30%
Poly(ethylene glycol) (MW = 200) (PEG)	40%	30%
3× TE buffer	35%	35%
Darocur 1173 photoinitiator	5%	5%

particles were removed from the refrigerator, rinsed 4 times in PTET (5× TET with 25% (v/v) PEG (400)), and allowed to sit at room temperature for 90 min. PTET was used to obtain better density-matching between the particles and the liquid medium in order to minimize the effects of sedimentation in the loading process. The PTET was sonicated for 1 min before use to eliminate polymer agglomerations that could disrupt particle flow. Once the particles were diluted to the appropriate concentration (10–20 particles μl^{-1}) with PTET, 20–30 μl of the mixture was loaded into a pipette-capped length of Tygon tubing. The pipette was then inserted into inlet 2. Particle types were never mixed together; each flow trial consisted of particles of identical shape and composition. A modified Eppendorf tube containing a 2% solution of food coloring in PTET was connected to inlet 1 *via* metal tubing. Tygon tubing was inserted through a hole in the Eppendorf cap to provide driving pressure. The tubing from the inlets was then attached to two separate pressure regulators (Omega) to provide independent control over the two streams. Flow devices were able to be reused up to 25 times without any decrease in performance. The compressed air source used to drive the flows was a plastic canister with a hand pump. Upon sufficient pumping, a two-way valve connecting the canister with the regulators was opened, thereby inducing flow. Pressures of 9 psi were able to be maintained for more than a minute using this simple setup.

High-speed imaging and analysis

Flow devices were mounted on an inverted microscope (TE2000U, Nikon) for visualization with 10× and 4× objectives. A high-speed Phantom camera (Vision Research) captured images at rates ranging from 4000 to 15 000 frames s^{-1}. Still images from the movies were analyzed using the Phantom Cine Viewer software (2.24 μm pixel^{-1} for 10× and 12.44 μm pixel^{-1} for 4×). Detection zone measurements of velocity, position, and alignment were always made 750 μm from the outlet to ensure consistency. A "successful" scan was defined to be one in which the horizontal distance between the center of any two holes in a given column of the code region was less than 5 μm. In addition, particles with any measurable lateral (y-direction) drift were deemed "unsuccessful" passages. This conservative definition of success is based on the PMT sampling rates (1 MHz) and excitation beam width (1–5 μm) that will be used in future one-dimensional scanning procedures. Quoted throughput values include both successful and unsuccessful particles, and unless otherwise noted, each flow trial involved the measurement of 100 particles.

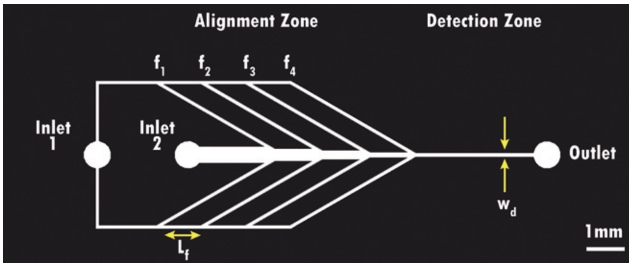

Fig. 2 Particle flow device. Schematic of a "4-focus" device, with four sets of side streams ($N = 4$), each separated by $L_f = 1000$ μm. Sections of constant width (450, 350, 250, 150, and 125 μm) are broken up by abrupt contractions. Sheath flow is introduced through inlet 1, while the particle-bearing fluid is introduced through inlet 2. The detection zone is the region in which the particle velocity, alignment, and position are evaluated to determine if a passage is successful. The measurement point was 750 μm from the outlet for all flow trials.

Results and discussion

The success of high-throughput microparticle scanning depends on *both* the fluidic channel design and the particle morphology. We took a three step approach to independently study these two facets of the project and optimize the process. First, using a canonical microparticle design we explored a variety of operating conditions and channel designs with the aim of minimizing clogging and disruptive particle–particle interactions in the detection zone. Next, particle size and composition were varied to explore the impact on alignment tendency and mechanical stability. Finally, the operational limits of a revised particle design suitable for bioassays were studied to maximize throughput and success rate while also maintaining a high degree of reproducibility; additional modeling and analysis of these particles were conducted to further understand the complexities of their behavior in high-speed flows.

Channel design

The effects of detection-zone width (w_d), side-stream number (N), side-stream spacing (L_f), and forcing pressures were studied for a fixed particle design. All particles used in channel optimization were photopolymerized from DA20 prepolymer, had dimensions of 270 × 90 × 33 μm, and featured 10 × 10 μm code holes spread evenly throughout the particle (Fig. 1a). The composition was selected based on its performance in earlier assay optimization studies,[15] while the hole design was chosen for its symmetry and for its use in alignment measurements. Loading concentration was fixed at 10 particles μl^{-1}.

Initial trials were performed with a simple channel design with one set of side streams ("1-focus device", $N = 1$). The central channel decreased in width from 500 to 100 μm at the meeting point of the side streams, producing a large velocity gradient in the flow direction. The detection zone was 2.3 mm in length, with $w_d = 100$ μm. The forcing pressures of the particle and sheath streams were matched, and they varied between 4 and 9 psi. Average particle velocities for this pressure range were between 10 and 30 cm s^{-1}. Analysis of the detection region revealed a tendency for particles to appear in clusters with poor alignment and slight deformations of the leading and trailing particle edges. Moreover, flow in the channel would temporarily decrease at times, producing wild variations in particle velocities over short periods of time.

These observations implied that the particles were jamming at the contraction point of the channel. Subsequent investigation of this region revealed periodic instances in which groups of 2–5 particles traveled closely together and lodged tightly in the contraction zone, thus impeding flow and leading to an accumulation and compression of particles. After 100–1000 ms, the elastic hydrogels would eventually squeeze past one another and eliminate the blockage, producing the clumps observed further downstream. It should be noted that the clogging *never* led to permanent (plastic) deformation. Particles collected in an exit reservoir did not exhibit any substantial structural abnormalities. Seeking a more gradual contraction with improved particle conditioning, additional trials with 2- and 3-focus devices with $w_d = 100$ μm and $L_f = 400$ μm were performed. The frequency and duration of the blockage events were reduced, but only by small amounts. Observations of the flow patterns in the 500 μm width region of 1-focus devices revealed a tendency for some particles to travel slowly along channel walls. Such behavior is consistent with the flow profile of a channel with a high aspect ratio, as discussed earlier. Although the same observations were made in the 500 μm wide regions of the 2- and 3-focus devices, the "wall-huggers" in these channels were reliably coerced off the wall prior to the detection zone by the local velocity increase created by the impinging side streams.

It was postulated that increasing L_f from 400 to 1000 μm would better enable particles to adopt a lengthwise flow orientation prior to the shorter contraction points at which clogs were occurring. This was based on the belief that rotation into the lengthwise orientation arose from a tendency for the particle to minimize the velocity gradient of the flow impinging upon it. The disordered flow patterns in the wakes of particles severely limited this effect, making congested areas less likely to produce well-aligned particles. Trials with larger L_f seemed to confirm this hypothesis. Based on observations of both upstream and detection zones, the longer residence time of the particles in the wide portions led to a nearly complete elimination of blockage events and drastic velocity variations in a modified 3-focus device with $L_f = 1000$ μm. However, deformations of particles traveling through the detection zone persisted, especially at higher forcing pressures. Particles approaching the final width contraction (200 to 100 μm) in the 3-focus device were seen to distort violently if they approached the contraction from a position far from the centerline of the channel. Furthermore, the small side gap between the particle and channel walls (5 μm on each side) led to a large pressure drop across the particle length and introduced substantial lift forces that compressed the particle in the direction perpendicular to flow and elongated it in the direction parallel to flow (~10% increase in length). Although such deformation could potentially increase the resolution of the proposed line scans, it was determined that future channels would have detection zones roughly twice as wide as the particle to preserve particle morphology by increasing bypass flow and lowering the pressure drop. In short, this study revealed the need for multiple sets of side streams separated by a sufficient distance, as well as a detection zone width that permitted substantial bypass flow for shape preservation.

Particle design

The control over hydrogel morphology and composition permitted by SFL is a valuable tool for design. The alignment of the tablet-shaped particles observed in initial experiments was far more reliable than that of additional morphologies that were also investigated (oblong particles with pointed ends, as well as tear-drop and bullet shapes). As a result, the 3-focus design with $L_f = 1000$ μm was adopted for the parametric study of the tablet-shaped particles. All studies detailed in this section were performed with $w_d = 150$ μm and a pressure of 9 psi for both inlets, leading to particle velocities of 25–35 cm s^{-1}.

The effect of particle aspect ratio (AR) was explored by flowing 90 μm wide particles (DA20 composition) with four different lengths: 190, 230, 270, and 310 μm. Flow trials involved measuring the lateral position and success rate of 100 particles of each type (Table 2). The position was calculated as the distance from the center of the particle to the centerline of the channel. It was observed that several of the shortest particles, AR = 2.11, exhibited significant lateral movement and had slanted front and rear edges upon reaching the detection zone (Fig. 3a). Particles with AR = 2.56 flowed more closely along the centerline of the channel and with virtually no lateral movement, but several had leading edges that were slightly blurred or compressed at driving pressures of 9 psi. Particles with AR = 3.00 exhibited drastic deformations (Fig. 3b–d), leading to the lowest success rate of the four particle types. In many instances, the front edge of the particle was bent towards one of the walls, thereby disrupting the alignment of the holes in the code region. This phenomenon is qualitatively similar to the deformations of tightly fitting red blood cells in two-dimensional channels. In the case of cells, the bending arises to reduce the driving pressure needed to sustain a certain cell velocity.[32] Several particles (10%) with this AR also exhibited curved side walls. The particles with AR = 3.44 suffered from none of the problems that plagued the other

Table 2 Effect of AR on particles in device with $N = 3$, $w_d = 150$ μm

Aspect ratio	Success rate	Mean distance from centerline (μm)	Main failure mode
DA20			
2.11	91%	4.5	Lateral movement
2.56	95%	2.6	Front deformation
3.00	82%	3.2	Front/back deformation
3.44	99%	1.4	None
DA30			
2.11	82%	9.2	Lateral movement
2.56	94%	6.9	Lateral movement
3.00	88%	6.5	Poor alignment
3.44	100%	3.6	None

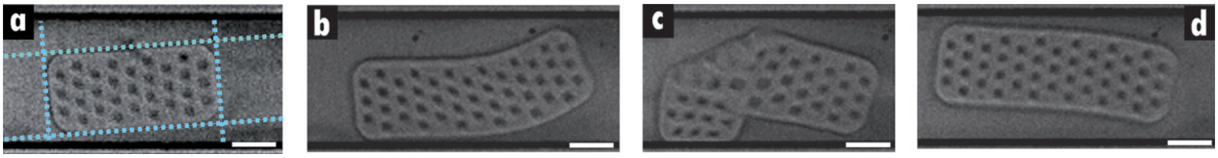

Fig. 3 Primary failure modes of DA20 particles in detection zone with $w_d = 150$ μm. (a) 190 × 90 μm particle (AR = 2.11) with poor alignment. (b–d) 270 × 90 μm particles (AR = 3.00) with drastic deformations that would preclude reading of the barcode. Scale bar in all images is 50 μm.

designs. The sole failure in this trial was one particle that was twisted into a U-shape.

The results of these trials indicated two potential sources of failure. At low AR, there was a reduced tendency to orient into and maintain a flow alignment that was conducive to scanning. As discussed earlier, the generation of lateral forces in the small side gap between the channel wall and the particle edge will tend to rotate the particle into an orientation such that the major axis of the particle is aligned with the centerline of the channel. This effect becomes more pronounced as the particle length-to-channel width ratio (b) becomes larger. Longer particles experience a larger net torque, and smaller side gaps generate greater lift. Meanwhile, failures of a different nature arose at more moderate AR. Particles with mid-range AR achieved the desired orientation and position within the detection zone, but they were more susceptible to deformations of their leading edges. A visual inspection of the particles entering the final contraction in the 3-focus device revealed that many of the particles of mid-range AR were poorly oriented and thus forced to bend significantly to enter the more narrow detection width. In contrast, particles with the lowest AR resisted such deformation and were able to enter with imperfect alignment due to their smaller size. Particles with the highest AR were already aligned sufficiently so that they did not experience distortion upon their entrance into the detection zone.

It is well known that the mechanical strength of a hydrogel depends to a great extent on the number and nature of the cross-links present.[33] By using a prepolymer with a higher proportion of crosslinking monomer (PEG-DA), it should be possible to generate hydrogel particles with higher cross-linking densities that are more resistant to deformation. The AR study was thus repeated with particles polymerized from DA30 prepolymer to investigate effects on flow characteristics (Table 2). From AFM measurements on particle regions *without* coding holes, the elastic modulus of the DA20 hydrogel was found to be 10.1 ± 0.4 kPa, while that of the DA30 hydrogel was found to be 19.6 ± 1.2 kPa (ESI).† The impact of the added rigidity of the DA30 particles was noticeable, with significantly less deformation at all values of AR. DA30 particles did not exhibit the bent leading edges, curved side walls, or compressions that plagued the softer DA20 particles. Observations of the final contraction revealed particles with no perceptible shape changes, in sharp contrast to the DA20 case.

While the higher cross-linking density solved one flow problem, it seemed to exacerbate the other. The stiffening of particles with ARs of 2.11 and 2.56 led to an increase in poorly aligned particles that were also more susceptible to moving laterally in the detection zone (Fig. 4). The use of DA30 raised the success rates of the two higher ARs, but actually led to a decrease in the success rates of the two lower ARs. In the case of DA30 particles with ARs of 2.11 and 2.56, the additional rigidity arising from higher cross-link density, when combined with the compact morphology, leads to a regime of rigid-body motion within the channel. This effectively eliminates the temporary hydrogel deformations induced by the surrounding focusing flow that play a significant role in coercing the particle into the preferred position and alignment. Any attempt to tune the flow behavior with this design parameter must balance the desire for structural integrity with the need for efficient focusing and orientation by hydrodynamic forces. Thus, the best particle design will have a high aspect ratio and a stiff gel network.

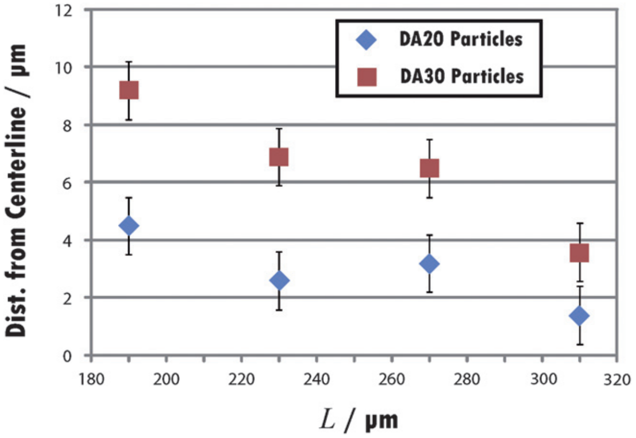

Fig. 4 Lateral position of particle (W = 90 µm) in detection zone with w_d = 150 µm. This plot demonstrates the difference in position for particles of different lengths and compositions. At all lengths, the softer DA20 particles exhibit superior positioning and a reduced tendency to move laterally. Longer particles are observed to settle into stable flow trajectories closer to the centerline than shorter particles. Each point represents 100 particles, and all measurements were made from the channel centerline to the centralmost point of the particle.

Barcoded particle design and optimization

The channel and particle motifs with the best performance characteristics were selected to create a flow-through system that could be operated reliably at high-throughput with hydrogel designs that were capable of extracting and displaying information from bioassays. Three different channel designs (A, B, C) were used (Table 3), each with L_f = 1000 µm. The shape and composition of the hydrogel particle were altered to ensure proper alignment, durability in high-velocity flows, and compatibility with bioassays. Using new masks and SFL, 9 µm × 9 µm holes were limited to one half of the particle, thus creating a "probe" region and a "code" region (Fig. 5a). Columns and rows of holes were separated by 9 µm. This design allows the capture and quantification of target(s) on one end and the display of probe identity on the other.[15] To create "bifunctional" particles, the code region was polymerized from DA30 to ensure mechanical stability, while the probe region was polymerized from DA20 to produce a pore size consistent with that featured on particles employed in high-sensitivity assays in previous work.[15,17] Furthermore, the use of DA20 imparted a flexibility that would aid in orientation within the channel, as seen in the earlier particle study. The new particles were 235 × 65 × 35 µm and featured a redesigned hole setup capable of 3072 distinct

Table 3 Channel parameters

Name	w_d (µm)	Side stream sets, N	Upstream widths (µm)
A	100	4	450, 350, 250, 150, 100
B	125	4	450, 350, 250, 150, 125
C	150	3	450, 350, 250, 150

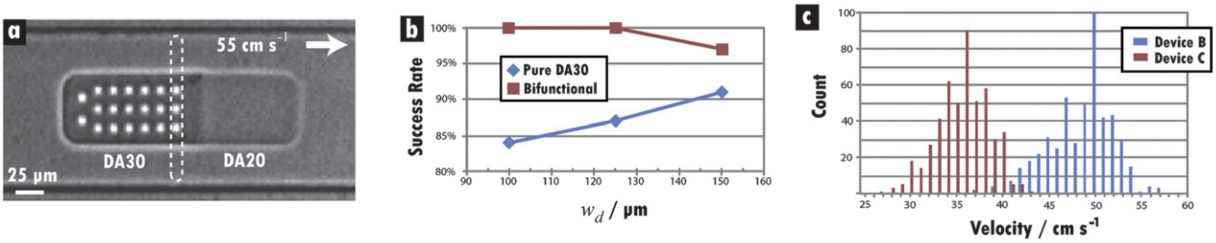

Fig. 5 Bifunctional barcoded particles. (a) Image from high-speed movie of bifunctional barcoded particle flowing “probe-first” at 55 cm s^{-1} from left to right in a channel with $w_d = 125$ μm. The dotted box around the first column of holes is drawn to indicate the thin excitation beam that will be employed in future 1-D line scans. Column and row spacings are 7 and 9 μm, respectively. (b) Plot showing superior performance of bifunctional design. Each point represents 100 particles. (c) Histogram of detection-zone velocities of 1000 bifunctional particles in devices B and C. The small spread of velocities for each device indicates a high degree of order and repeatability. Results are compared from trials run in five B and five C devices with five different particle batches. The tails on the left side of each spike can be attributed to the small percentage (15–20%) of particles that flowed “code-first.” For the bifunctional design, these particles were typically 10% slower than their probe-first counterparts.

codes. The AR of this design (3.62) was higher than any used in previous flow trials.

Bifunctional design. To evaluate this new design, bifunctional particles were flowed through the three channel types at loading concentrations of 10 particles μl^{-1}, and their performance was compared to that of particles with probe and code regions both synthesized from DA30. Higher success rates were recorded for the bifunctional particles in all three channels (Fig. 5b). Bifunctional particles also flowed more closely along the centerline than their pure-DA30 counterparts in all channel types, with the best positioning achieved in design C. With the asymmetric morphology, a preference for “probe-first” flow was observed, with 91% of bifunctional and 79% of pure-DA30 particles doing so. In addition, higher velocities (35–60 cm s^{-1}) were recorded for these slender particles. Compared to the previously used 90 μm wide design, the 65 μm wide design provided larger side gaps that effectively reduced the pressure drop across the particle, thereby diminishing the tendency to deform in the detection region. For the 600 total hydrogels analyzed, probe-first particles traveled ~10% faster than code-first particles, with a larger difference being measured for the pure-DA30 design.

Hole spacing. The effect of hole spacing was investigated, again using the same three channel designs. Seeking to increase throughput, the loading concentration was increased from 10 to 15 particles μl^{-1} for these trials. Bifunctional particles with column spacings of 9, 7, and 5 μm were studied (all row spacings remained 9 μm). Shorter column spacings reduce the particle area needed for coding and thus increase the area available for probe immobilization. However, the desire to minimize the code area must be balanced by the need to maintain structural integrity. Nine trials with bifunctional particles of the three spacings in the three channels revealed a noticeable reduction in success rate for holes with 5 μm spacing. For the 900 hydrogels studied, the average success rates of the 9, 7, and 5 μm spacings were 97%, 99%, and 88%, respectively. Most failures of the smallest spacing were due to large compressions of holes in particles traveling code-first. Mean throughput at the higher loading concentration was 29 particles s^{-1}, while mean velocity was 51 cm s^{-1}.

Repeatibility. The high success rates achieved in devices B and C (100% and 99%, respectively) with 7 μm spacing were explored further by conducting additional trials. Five new batches of bifunctional particles with the spacing were synthesized, and five devices of each type were constructed. To investigate the reproducibility of the earlier results, each batch was sent through one of the five sets of devices (*i.e.*, batch 1 through B-1 and C-1, batch 2 through B-2 and C-2, *etc.*) at a loading concentration of 15 particles μl^{-1}. The results of these trials (Table 4) indicated a high degree of repeatability, including inter-trial COVs less than 4% for the mean velocity, as well as mean success rates over 99%. This uniformity of particle speed (Fig. 5c) is crucial for high-fidelity signal analysis and signifies the establishment of well-ordered flows with minimal particle–particle interactions. As in earlier trials, particles preferentially adopted a probe-first orientation by the time they had entered the detection zone, with 76% flowing in this manner in B compared to 80% in C.

Table 4 Optimized particle[a] results for channels B and C at various loading concentrations

Loading concentration (particles μl^{-1})	Channel type	Number of trials[b]	Mean success rate	Mean throughput (s^{-1})	Mean velocity (cm s^{-1})	Inter-trial velocity COV	Percentage probe-first
15	B	5	99.8%	30.2	46.3	3.29%	84.4%
	C	5	99.2%	24.9	35.0	3.91%	84.6%
17.5	B	5	98.4%	40.2	48.1	2.02%	75.6%
	C	5	98.8%	35.4	35.4	1.44%	79.8%
20	B	1	92%	47.4	50.8	NA	86%
	C	1	91%	40.3	38.5	NA	71%

[a] Bifunctional design with AR = 3.62 and 7 μm column spacing. [b] Each trial involved the measurement of 100 particles. Thus, the total number of particles represented in this table is 2200.

Loading concentration. In order to maximize throughput, an attempt was made to determine the highest loading concentration that could still produce well-ordered, single-file flows. A reproducibility study similar to the one just described was conducted at a loading concentration of 17.5 particles μl^{-1}. Once again, a high degree of repeatability was achieved (Table 4), with a minor success-rate decrease that was outweighed by a noticeable increase in mean throughput. As in the previous study, device B performed slightly better, with a higher mean throughput. Trials were then performed at 20 particles μl^{-1}. At this concentration, a more significant drop-off in the success rate occurred (Table 4), with crowding in the channel significantly disrupting the upstream focusing and even leading to the partial overlap of particles in the detection region. It was concluded that the increase in throughput at 20 particles μl^{-1} was not worth the decrease in success rate, and the maximum concentration was set at 17.5 particles μl^{-1}.

Barcoded particle flow analysis

The hydrodynamic forces acting on the barcoded particles in the detection region of device B were explored by applying eqn. (1)–(5) to the nearly unidirectional side-gap flow to determine the torque involved in lengthwise alignment (ESI†). As expected, the torque about a central point on the particle's trailing edge increased as the deviation from lengthwise orientation grew (Fig. 6a). This torque always acted to restore the lengthwise orientation, and its magnitude was greater for particles with higher values of b (particle length-to-channel width ratio). This trend reinforces earlier observations regarding alignment tendencies and particle dimensions. For the case $b = 1.88$, results of the lubrication approximation agree well with the torques calculated for various values of θ using 2-D COMSOL simulations (Fig. 6b, ESI†).

To further understand the flow in B, the orientation of particles was recorded by measuring the *acute* angle between the major axis of the particle and the centerline of the channel (θ) as particles moved through the upstream contraction points (Fig. 7a). An indication of alignment tendency can be obtained by measuring the standard deviation in this angle at the end of each constant-width region for a collection of 85 particles (Fig. 7b). The results indicate a nearly linear decrease in deviation as the channel width decreases for both of the orientations. The larger deviations in θ for code-first particles suggest this orientation is not driven to alignment in the flow as strongly as probe-first particles (ESI, Video S3†). Indeed, of the 85 particles studied, four switched from code-first to probe-first during flow, while none made the transition from probe-first to code-first. A closer examination of one particle of each orientation reinforces this hypothesis. For each frame of video, the *full* angle (*i.e.*, 0–360°) between the long axis and the centerline (φ) was measured to preserve orientation information, with code-first corresponding to $\varphi = 0°$ and φ increasing in the counter-clockwise direction (Fig. 7c). Despite starting only 20° from a lengthwise orientation, the code-first particle nearly moves into a widthwise orientation before rotating back into a code-first alignment that oscillates quite dramatically as the channel width approaches 150 μm. Meanwhile, the probe-first particle behaves in a much more controlled and predictable manner, with a rapid transition from widthwise to lengthwise orientation before a relatively mild oscillation about $\varphi = 180°$.

These analyses provide insight into the preferential orientation that was observed in every trial with the half-probe/half-code particles, including those in which both regions were polymerized from DA30. Of the 3200 bifunctional particles analyzed in A, B, and C devices, 83% flowed probe-first, compared to 79% of the 300 pure-DA30 particles. This indicates that the flexibility difference in the bifunctional design plays, at most, a minor role in the preference. The measurements of rotational tendency in the upstream region imply that the resistance to fluid flow in the thin height gaps (each ∼1–2 μm) above and below the code region is different from the resistance in the height gaps above and below the probe. This disparity can be observed directly by comparing the lateral wobbles of a code-first particle to the smooth, settled flow of a probe-first particle in the upstream regions of a channel (Fig. 7c). While it is tempting to attribute this resistance difference to the relative stiffness of the code region, the data from the pure-DA30 trials refute this claim. The holes that constitute the graphical code are the only other source of asymmetry in the particle and thus appear to give rise to the resistance difference. It seems that the flow pattern and the resulting pressure gradient along the length of the particle in the height gap depend on whether the holes are on the leading or the trailing edge of the particle. This hypothesis is supported by

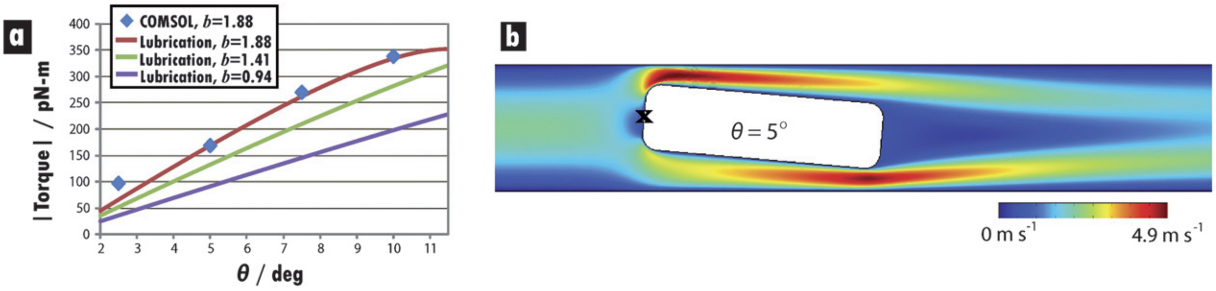

Fig. 6 Hydrodynamic forces on misaligned particles. (a) Plot of torque magnitude calculated for misaligned particle centered in detection zone with $w_d = 125$ μm. Torque is calculated about the central point on the trailing edge of the particle (marked by a black cross in (b)), based on experimental observations of particle rotation. As expected, higher deflection angles and higher values of b lead to larger torques that restore the particle to a lengthwise orientation. Lubrication analysis shows excellent agreement with torques calculated using 2-D COMSOL simulations of flow profiles (b) for the commonly investigated situation of $b = 1.88$ (*i.e.*, particle length of 235 μm and channel width of 125 μm). Calculations are based on a 1.5 psi drop across a 700 μm long detection zone containing a single particle. Re of the flow upstream of the particle is ≈ 15.

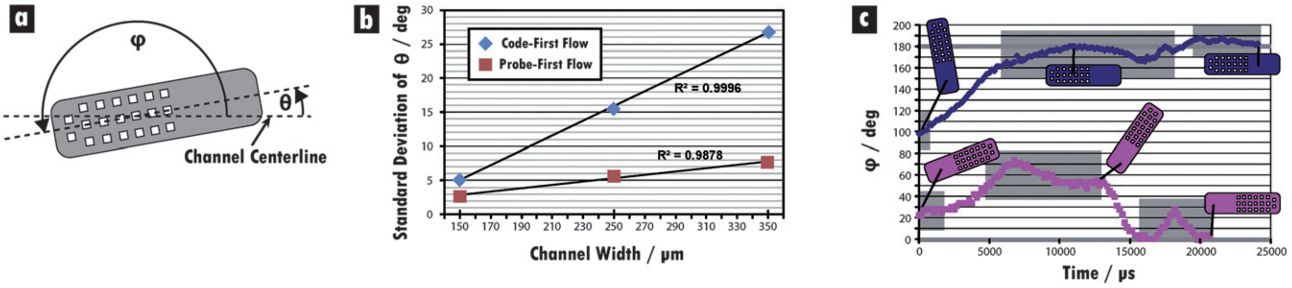

Fig. 7 Upstream rotation analysis in device B. (a) Schematic depicting the two angles of interest. (b) Plot of deviation of θ with channel width in the upstream region for particles that flow code- or probe-first. The larger deviation exhibited by the code-first particles suggests that such an orientation is less stable than the probe-first orientation. Measurements were taken at the end of the corresponding constant-width region prior to contraction. (c) Plot of φ over the course of the travels of two particles through the upstream region. The probe-first orientation is seen to be achieved in a smoother and more predictable fashion than the code-first orientation, again suggesting that the probe-first orientation is more stable. While the probe-first particle experiences limited disruptions in the regions of constant width (shaded boxes), the code-first particle experiences two sharp alterations in alignment. From left to right, the constant-width regions measure 350, 250, and 150 μm, respectively.

the observed velocity disparity between code- and probe-first particles noted earlier for bifunctional particles as well as pure-DA30 particles.

Conclusions

We have shown that a plurality of sufficiently spaced side-focusing streams, a detection zone of ample width, and a moderate particle loading concentration are crucial for the high-throughput flow alignment of graphically encoded hydrogel microparticles. In addition, the reliable alignment of soft particles in high-speed flows (without deformation or clogging) is greatly enhanced by simultaneously optimizing the mechanical properties and morphology of the particles to ensure efficient focusing by hydrodynamic forces while still maintaining overall structural integrity in areas of high shear. The high throughputs achieved in the optimized design of our microfluidic system (40 particles s^{-1}) compare favorably with those of currently available technologies for analyzing hard-sphere suspension arrays. The use of multiple probe strips on each particle in our setup has the potential to greatly augment this processing capacity in future work.

The next step in the development of this platform is the implementation of a PMT for the detection of the fluorescence emitted by the passing particles. The single-color detection scheme made possible by the graphical encoding of probe identity should make the platform easier and less expensive to operate than existing suspension array cytometers. Furthermore, the large code library of the method described here permits the pooling of samples prior to scanning, a step which can greatly reduce processing times for assays.

Acknowledgements

The authors would like to thank Dae Kun Hwang for helpful discussions, Octavio Hurtado and the BioMEMS Resource Center for use of their cleanroom and Phantom camera, and Adam Zeiger for help with AFM measurements. We acknowledge support from grant R21EB008814 from the National Institute of Biomedical Imaging and Bioengineering, National Institutes of Health, the Desphande Foundation and the Royal Society of Chemistry Journal Grant for International Authors.

References

1 W. Kalow, *The Pharmacogenomics Journal*, 2006, **6**, 162–165.
2 N. M. Verrills, *Clin. Biochem. Rev.*, 2006, **27**, 99–116.
3 D. Peck, E. D. Crawford, K. N. Ross, K. Stegmaier and T. R. Golub, *Genome Biol.*, 2006, **7**, Article R61.
4 D. Zichi, B. Eaton, B. Singer and L. Gold, *Curr. Opin. Chem. Biol.*, 2008, **12**, 78–85.
5 S. P. Fodor, R. P. Rava, X. C. Huang, A. C. Pease, C. P. Holmes and C. L. Adams, *Nature*, 1993, **364**, 555–556.
6 D. A. A. Vignali, *J. Immunol. Methods*, 2000, **243**, 243–255.
7 R. Wilson, A. R. Cossins and D. G. Spiller, *Angew. Chem., Int. Ed.*, 2006, **45**, 6104–6117.
8 M. Evans, C. Sewter and E. Hill, *Assay Drug Dev. Technol.*, 2003, **1**, 199–207.
9 Z. Zhi, Y. Morita, Q. Hasan and E. Tamiya, *Anal. Chem.*, 2003, **75**, 4125–4131.
10 R. J. Fulton, R. L. McDade, P. L. Smith, L. J. Kienker and J. R. K. Jr, *Clin. Chem.*, 1997, **43**, 1749–1756.
11 K. L. Kellar and M. A. Iannone, *Exp. Hematol.*, 2002, **30**, 1227–1237.
12 S. R. Nicewarner-Pena, R. G. Freeman, B. D. Reiss, L. He, D. J. Pena, I. D. Walton, R. Cromer, C. D. Keating and M. J. Natan, *Science*, 2001, **294**, 137–141.
13 M. Sha, I. Walton, S. Norton, M. Taylor, M. Yamanaka, M. Natan, C. Xu, S. Drmanac, S. Huang, A. Borcherding, R. Drmanac and S. Penn, *Anal. Bioanal. Chem.*, 2006, **384**, 658–666.
14 A. M. Kolchinsky, D. A. Gryadunov, Y. P. Lysov, V. M. Mikhailovich, T. V. Nasedkina, A. Y. Turygin, A. Y. Rubina, V. E. Barsky and A. S. Zasedatelev, *Mol. Biol.*, 2004, **38**, 4–13.
15 D. C. Pregibon, M. Toner and P. S. Doyle, *Science*, 2007, **315**, 1393–1396.
16 D. Dendukuri, S. S. Gu, D. C. Pregibon, T. A. Hatton and P. S. Doyle, *Lab Chip*, 2007, **7**, 818–828.
17 D. C. Pregibon, PhD Thesis, Massachusetts Institute of Technology, 2008.
18 P. Crosland-Taylor, *Nature*, 1953, **171**, 37–38.
19 K. L. Kellar and J. P. Douglass, *J. Immunol. Methods*, 2003, **279**, 277–285.
20 E. Morgan, R. Varro, H. Sepulveda, J. A. Ember, J. Apgar, J. Wilson, L. Lowe, R. Chen, L. Shivraj, A. Agadir, R. Campos, D. Ernst and A. Gaur, *Clin. Immunol.*, 2004, **110**, 252–266.
21 D. Huh, W. Gu, Y. Kamotani, J. B. Grotberg and S. Takayama, *Physiol. Meas.*, 2005, **26**, R73–R98.
22 T. D. Chung and H. C. Kim, *Electrophoresis*, 2007, **28**, 4511–4520.
23 S. Chung, S. J. Park, J. K. Kim, C. Chung, D. C. Han and J. K. Chang, *Microsyst. Technol.*, 2003, **9**, 525–533.
24 A. S. Yang and W. H. Hsieh, *Biomed. Microdevices*, 2006, **9**, 113–122.
25 C. Simonnet and A. Groisman, *Anal. Chem.*, 2006, **78**, 5653–5663.

26 C.-C. Chang, Z.-X. Huang and R.-J. Yang, *J. Micromech. Microeng.*, 2007, **17**, 1479–1486.
27 M. Faivre, M. Abkarian, K. Bickraj and H. A. Stone, *Biorheology*, 2006, **43**, 147–159.
28 D. Halpern and T. W. Secomb, *Journal of Fluid Mechanics*, 1991, **231**, 545–560.
29 D. Halpern and T. W. Secomb, *Journal of Fluid Mechanics*, 1992, **244**, 307–322.
30 J. M. Fitz-Gerald, *Proceedings of the Royal Society of London B*, 1969, **174**, 193–227.
31 W. M. Deen, *Analysis of Transport Phenomena*, Oxford University Press, New York, 1st edn., 1998, 270–278.
32 T. W. Secomb and R. Skalak, *Microvascular Research*, 1982, **24**, 194–203.
33 K. S. Anseth, C. N. Bowman and L. Brannon-Peppas, *Biomaterials*, 1995, **17**, 1647–1657.